Signal Processing 176 (2020) 107708

Contents lists available at ScienceDirect

Signal Processing

journal homepage: www.elsevier.com/locate/sigpro

Unsupervised quaternion model for blind colour image quality assessment

Leyuan Wu[a], Xiaogang Zhang[a,*], Hua Chen[b], Yicong Zhou[c]

[a] College of Electrical and Information Engineering, Hunan University, Changsha, Hunan, China
[b] College of Computer Science and Electronic Engineering, Hunan University, Changsha, Hunan, China
[c] Faculty of Science and Technology, University of Macau, Taipa, Macau

ARTICLE INFO

Article history:
Received 17 February 2020
Revised 11 June 2020
Accepted 15 June 2020
Available online 7 July 2020

Keywords:
Colour image processing
Natural scene statistical
Quaternion representation
Unsupervised blind image quality assessment

ABSTRACT

Without the limitations of labelled distorted images for training, the unsupervised blind colour image quality assessment (UBCIQA) model shows excellent generalization performance. However, existing UBCIQA methods fail to consider the correlation between different colour channels. This paper proposes an efficient UQBCIA algorithm. Placing R, G, and B channels of a colour image into the three imaginary parts of a quaternion, the proposed UQBCIA obtains the quaternion representation of a colour image, which allows UQBCIA to process the colour image as a whole while keeping its three colour channels dependent. The naturalness, structural and texture statistic features are then extracted to fit a multivariate Gaussian (MVG) model. The quality of the test colour image is calculated as the MVG distance between the fitted pristine images and the test image. The proposed method is evaluated from three aspects: (1) prediction accuracy, (2) computational complexity and (3) robustness on five colour databases. The results demonstrate that the proposed UQBCIA algorithm outperforms state-of-the-art unsupervised and classical supervised BIQA methods.

1. Introduction

As photography becomes a fashionable way to record our daily life and express our emotions, the number of colour images has been exploding in recent years. Since the colour image is expected to obtain maximum visual qualities in imaging, it is important to quantitatively estimate the distortion level of a colour image. Under these conditions, the objective image quality assessment (IQA) algorithms, which assess the degradation of a distorted image by establishing mathematical models to simulate subjective opinion scores, have attracted much attention in the past decades [1].

There are three types of objective IQA models depending on the reference level of clear image. Full-reference IQA needs all information of the reference image, and calculates the similarity between the reference image and distorted image in pixel-wise [2]. To reduce the dependence on the reference image, reduced-reference IQA extracts some effective features from the image using some image representation methods (e.g., perceptual hashing method [3]), and calculates the feature distance between the reference and distorted images for quality evaluation [4,5]. Unfortunately, the reference image is usually inaccessible in most scenes. In this paper, we focus on the no-reference (NR) field, which is also called blind IQA (BIQA). Early BIQA models mainly concentrated on distortion-specific methods, which are designed for specific types of distortion [6,7]. However, in most applications, the distortion types are varied and inaccessible in advance. Therefore, distortion-specific methods have limited applications.

In recent years, many studies have examined general-purpose NR-IQA to assess the wild range of distortion types. According to whether subject scores are required in the construction process of model, general-purpose IQA algorithms can be classified into supervised and unsupervised methods. Supervised methods can be further classified into classical machine learning-based methods [8–14] and deep learning-based methods [15–17]. For classical machine learning-based methods, after some hand-crafted quality-aware features are extracted, regression models are built by using machine learning methods to map the extracted features to subjective quality scores. For deep learning-based methods, the features are extracted by deep learning algorithms automatically. The trained model behaves well when fully trained. However, the trained model will have limited performance when the test image is distorted by untrained distortions (i.e., the distortion types are not included in training). Therefore, these supervised methods have weak generalization capability and the trained model

* Corresponding author.
E-mail addresses: wly1992@hnu.edu.cn (L. Wu), zhangxg@hnu.edu.cn (X. Zhang), anneychen@126.com (H. Chen), yicongzhou@um.edu.mo (Y. Zhou).

https://doi.org/10.1016/j.sigpro.2020.107708
0165-1684/

is difficult to extend to other IQA fields in practical application. Considering that high quality natural images have strong "naturalness" and are easy to obtain, unsupervised methods [18–22] have been proposed by extracting some natural scene statistics features from pristine images to learn a multivariate Gaussian (MVG) model that serves as the "clear" image. For a test image, the quality score is calculated as the distance between the learned MVG model and the MVG model calculated from the test image. Unsupervised methods do not need large numbers of labelled distorted images for training, and therefore show a better generalization performance than supervised methods [21,22]. Although unsupervised methods are more applicable in practice, they have not yet been adequately studied. In this paper, we further investigate the unsupervised model and propose an unsupervised method for BIQA.

The colour information in an image is widely used in our daily life, as our human eyes can readily identify a colour object [23]. How to process the colour information in an image is a basic yet important task. According to scientific studies, colour information accounts for 80% of the initial sighting by the human eye, and 50% of the perceived colour information will still remain after 2 min [24]. Furthermore, most of the existing images are colour images. Therefore, incorporating the colour information into IQA modelling is essential. Basically, there are three strategies used for colour processing in IQA. The first strategy is converting the colour image into greyscale and extracting features on it [8–13,18–20,22], such as Blind Image Quality Index (BIQI) [8], Blind Image Spatial QUality Evaluator (BRISQUE) [12], Natural Image Quality Evaluator (NIQE) [20], and Structure Naturalness and Perception NIQE (SNP-NIQE) [22]. This strategy, however, will cause colour information loss. The model will be less effective if the image is affected by colour distortion types.

The second strategy is to extract features separately on each channel of the colour image, and then combine them for more comprehensive modelling. In Integrated Local NIQE (IL-NIQE) [21], Lin et al. calculated the gradient maps from the R, G and B channels, separately. This strategy was also adopted by Wu et al. in the distortion Type Classification Label Transfer (TCLT) [14] model. They extracted discrete cosine transform, wavelet and spatial features from the R, G, B channels of a colour image, respectively. Experiments have shown that this approach can boost the performance of an algorithm, but the computational complexity also increases greatly. Furthermore, the correlations of the colour channels are ignored [25].

Because a colour image has three channels and a quaternion has three imaginary components, the strategy is proposed by encoding the RGB channels into the three imaginary parts of the quaternion. With quaternion representation (QR), the colour image can be processed as a whole while keeping its three colour channels dependent. Through extracting features on the quaternion matrix, the correlations between different colour channels can be well preserved without increasing the computational complexity [26]. Such strategy is broadly used in colour image processing. Examples include colour image classification [27], colour face image recognition [28], colour image denoising [29], etc.. Some studies have also been done on colour image quality evaluation field using QR. In [30], Wang et al. represented the colour image in quaternion, and followed a singular value decomposition. The quality of the test image was measured as the angle between the singular value feature vectors derived from the reference image and test image. In [31], Chen et al. established hybrid phase congruency for IQA through quaternion Gabor wavelets. In [32], as an extension of Structural SIMilarity (SSIM) [2], Kolaman et al. measured the structural similarity between a reference image and the distorted image in quaternion domain, and referred to this method as Q-SSIM.

Existing QR-based IQA models are all full-reference methods. Considering the excellent merit of QR in processing colour images, we establish an unsupervised quaternion blind colour image quality assessment (UQBCIA) model via QR in this paper. The colour image is initially represented as a quaternion. Then, quality-aware features, including naturalness statistical features, structure statistical features and texture statistical features are extracted to establish a MVG model. Finally, the quality of a distorted image is calculated by measuring the MVG variations between the fitted of distorted image and the fitted of pristine natural images. As the extension work of NIQE, IL-NIE and SNP-NIQE, the proposed model is named as Q-NIQE.

In summary, this paper offers the following contributions:

1. Existing BIQA methods, whether converting the colour image into greyscale, or extracting features on each channel of the colour image, are far from an ideal colour image processing method. To solve this problem, this paper represents the colour image as a pure quaternion, and extracts some statistical features for IQA modelling. To the best of our knowledge, existing QR-based IQA methods are FR. We are the first to process the colour image with QR in the NR field.
2. Based on the features extracted from the quaternion, we propose a UQBCIA model. The proposed method can process colour image effectively without greatly increasing computational cost. The experiments demonstrate that our model has a higher prediction accuracy than state-of-the-art unsupervised BIQA methods and classical supervised BIQA methods. Specially, the proposed model has a much higher prediction accuracy for real and multiple distortions, which indicates that our model is more efficient in application.

2. Quaternion algebra

The quaternion algebra extends the one imaginary part in complex algebra to three parts [33], and the mathematical representation is:

$$\ddot{Q} = q_0 + q_1 i + q_2 j + q_3 k \quad q_0, q_1, q_2, q_3 \in R \tag{1}$$

Two points on a variable denote the variable is a quaternion. *i, j*, and *k* are the fundamental quaternion units and subject to the following rules:

$$i^2 = j^2 = ijk = -1, \quad ij = -ji = k \tag{2}$$

The quaternion can also be represented as $\ddot{Q} = (q_0, q_1, q_2, q_3) = [S(\ddot{Q}), V(\ddot{Q})]$ with the scalar part $S(\ddot{Q}) = q_0$, and the vector part $V(\ddot{Q}) = \{q_1, q_2, q_3\}$. The conjugate of $\ddot{Q}$ is defined as:

$$\ddot{Q}^* = q_0 - q_1 i - q_2 j - q_3 k \tag{3}$$

The norm of the quaternion can be obtained via:

$$|\ddot{Q}| = \sqrt{\ddot{Q} \cdot \ddot{Q}^*} = \sqrt{q_0^2 + q_1^2 + q_2^2 + q_3^2} \tag{4}$$

The multiplication between a scalar γ and a quaternion is computed as:

$$\gamma \ddot{Q} = \gamma q_0 + \gamma q_1 i + \gamma q_2 j + \gamma q_3 k \tag{5}$$

For two quaternions $\ddot{X} = x_0 + x_1 i + x_2 j + x_3 k$ and $\ddot{Y} = y_0 + y_1 i + y_2 j + y_3 k$, the multiplication between them is defined as:

$$\begin{aligned} \ddot{X}\ddot{Y} &= (x_0 + x_1 i + x_2 j + x_3 k)(y_0 + y_1 i + y_2 j + y_3 k) \\ &= (x_0 y_0 - x_1 y_1 - x_2 y_2 - x_3 y_3) \\ &\quad + (x_0 y_1 + x_1 y_0 + x_2 y_3 - x_3 y_2) i \\ &\quad + (x_0 y_2 - x_1 y_3 + x_2 y_0 + x_3 y_1) j \\ &\quad + (x_0 y_3 + x_1 y_2 - x_2 y_0 + x_3 y_1) k \end{aligned} \tag{6}$$

Define '$\bullet$' as the dot product operator and '$\otimes$' as the cross product operator. Then, the equation above can be rewritten as:

$$\begin{aligned} S(\ddot{X}\ddot{Y}) &= S(\ddot{X})S(\ddot{Y}) - V(\ddot{X}) \bullet V(\ddot{Y}) \\ V(\ddot{X}\ddot{Y}) &= S(\ddot{X})V(\ddot{Y}) + S(\ddot{Y})V(\ddot{X}) + V(\ddot{X}) \otimes V(\ddot{Y}) \end{aligned} \tag{7}$$

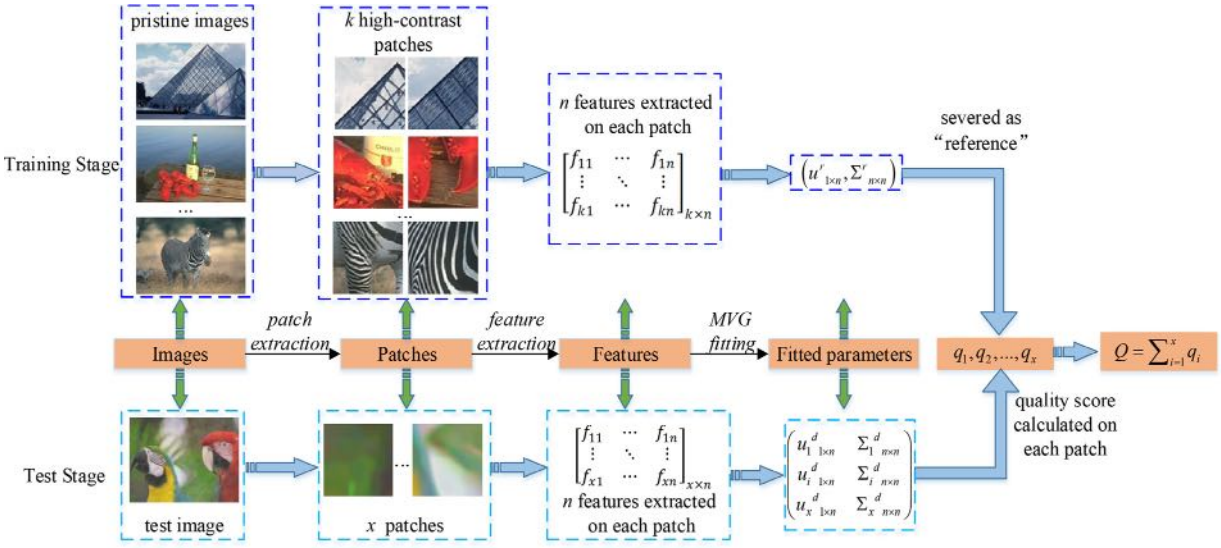

Fig. 1. The framework of the proposed method.

For two pure quaternions, i.e., $S(\ddot{X}) = S(\ddot{Y}) = 0$, the multiplication between them can be computed as:

$$\begin{aligned} S(\ddot{X}\ddot{Y}) &= -V(\ddot{X}) \bullet V(\ddot{Y}) \\ V(\ddot{X}\ddot{Y}) &= V(\ddot{X}) \otimes V(\ddot{Y}) \end{aligned} \tag{8}$$

The multiplication of two pure quaternions is not the dot product of them. Therefore, feature extraction in the quaternion domain does not simply combine the features extracted from each channel of an RGB colour image. This conclusion is proven in Q-SSIM. For more information, please refer to [32].

3. The proposed unsupervised BIQA method

The framework of the proposed method is first presented in this section. Then, as the core of this method, the feature extraction process is presented. Finally, a validation is conducted to investigate the effectiveness of the extracted features.

3.1. Framework of the proposed method

The framework of the proposed method is illustrated in Fig. 1. First, to capture the local degradation of an image, the image is decomposed into a set of non-overlapped patches. The patch size is fixed as 72 in our model. Then, some quality-aware features, including the naturalness statistical features, structural statistical features and texture statistical features are extracted on each patch after QR, and fitted into a MVG model as:

$$M(f; u, \Sigma) = \frac{1}{(2\pi)^{l/2}|\Sigma|^{1/2}} \exp\left(-\frac{1}{2}(f-u)^T \Sigma^{-1}(f-u)\right) \tag{9}$$

where μ, Σ are two fitting parameters. Denote μ_r, Σ_r and μ_d, Σ_d are the MVG parameters fitting from pristine patches and the test patches, respectively. Last, the quality of the test image patches are calculated as the distance between the MVG model derived from pristine patches and the MVG model derived from test patches:

$$Q = \sqrt{(\mu_d - \mu_r)^T \left(\frac{\Sigma_d + \Sigma_r}{2}\right)^{-1} (\mu_d - \mu_r)} \tag{10}$$

The final quality score of the test images is expressed as the mean value of quality scores on each patch.

Fig. 2. Simple pristine images selected for learning the pristine MVG model. The first, second, third, and last rows are the people, architectures, animals and natural landscapes images, respectively.

To train the "clear" image against all distorted images, we select 108 pristine images from Berkeley image segmentation database [34]. The pristine images can be separated into 4 categories: people, architectures, animals and natural landscapes. Fig. 2 illustrates some sample images that used in training. To illustrate the dependence from the pristine images of our model, we also trained our model using the pristine images from NIQE and IL-NIQE, and the results are shown in Section 4. Additionally, to better learn the characteristics of pristine images, only the patches containing high-contrast are selected for learning. In implementation, we calculate the contrast of each pixel using Eq. (14), and the mean value is used to denote the contrast level of the patch. Only the contrast level of the patch exceeding the threshold we set is used for learning the MVG model. The threshold is fixed as 80% of the maximum contrast level in our model. To reduce the dimension of the extracted features, PCA is applied before learning the MVG model, and the parameters are fixed as IL-NIQE [21].

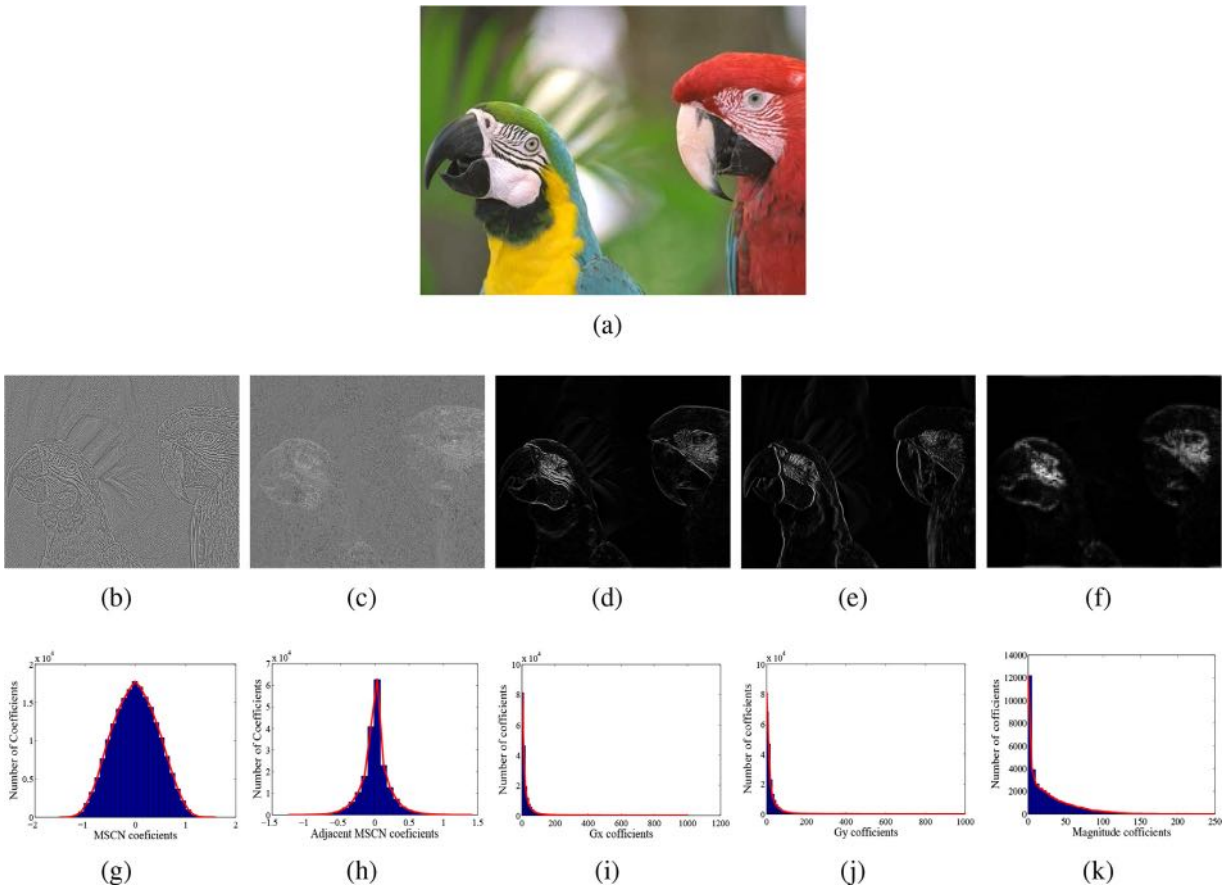

Fig. 3. The feature maps and their distributions. (a) is an image from TID2013 database. the second row are the feature maps of (a) with (b) *QMSCN* map, (c) Adjacent *QMSCN* map, (d) QG_x map, (e) QG_y map, (f) *QGabor* map. The last row are the distributions of the second row in order.

3.2. Quaternion naturalness statistical modelling

Naturalness is confirmed to be an important property for a natural image, and is usually characterized by modelling the locally mean subtracted and contrast normalized (MSCN) coefficients and the products of pairs of adjacent MSCN coefficients [20–22,35]. In this paper, the MSCN and adjacent MSCN are derived from the quaternion domain. A colour image I, can be represented in pure quaternion as [36]:

$$\ddot{I} = Ri + Gj + Bk \tag{11}$$

where R, G and B are the three channels of I. The MSCN coefficients in quaternion domain are calculated as:

$$QMSCN(x,y) = \frac{|\ddot{I}(x,y)| - |\ddot{u}(x,y)|}{\sigma(x,y) + 1} \tag{12}$$

where x and y are spatial coordinates. $|\cdot|$ denotes the norm operation. $\ddot{\mu}$ and σ denote the local mean and standard deviation respectively, which can be calculated as:

$$\ddot{\mu}(x,y) = \sum_{m=-M}^{M}\sum_{n=-N}^{N} \ddot{w}_{m,n}\ddot{I}(x+m, y+n) \tag{13}$$

$$\sigma(x,y) = \sqrt{\sum_{m=-M}^{M}\sum_{n=-N}^{N} \ddot{w}_{m,n}(|\ddot{I}(x+m, y+n)| - |\ddot{\mu}(x,y)|)^2} \tag{14}$$

where $\ddot{w}$ denotes a quaternion Gaussian window in unit-volume.

To visually show the distribution of the QMSCN coefficients, Fig. 3(a) shows an image from TID2013 database [37], and Fig. 3(b) is the QMSCN map. (g) is the distribution of (b). It can be seen that the distribution of the QMSCN coefficients followed a GGD with a zero-mean [38], which is defined as:

$$f_{GGD}(x;\alpha,\beta) = \frac{\alpha}{2\beta\Gamma(1/\alpha)} \exp\left(-\left(\frac{x}{\beta}\right)^{\alpha}\right) \tag{15}$$

where $\Gamma(\cdot)$ is the gamma function as follows:

$$\Gamma(x) = \int_0^{\infty} t^{x-1}e^{-t}\,dt, x > 0 \tag{16}$$

The obtained distribution parameters α and β are incorporated as the quality-aware features.

The products of pairs of adjacent QMSCN coefficients along 0°, 45°, 90°, 135° are also naturalness indicators, which can be obtained through [12]:

$$\begin{aligned} h(x,y) &= QMSCN(x,y)QMSCN(x,y+1) \\ d_1(x,y) &= QMSCN(x,y)QMSCN(x+1,y+1) \\ v(x,y) &= QMSCN(x,y)QMSCN(x+1,y) \\ d_2(x,y) &= QMSCN(x,y)QMSCN(x+1,y-1) \end{aligned} \tag{17}$$

Fig. 3(c) and (h) illustrates the adjacent QMSCN map in the h orientation and its distributions of it. This distribution can be well modelled by an asymmetric GGD (AGGD) in zero mode [39]:

$$f_{AGGD}(x;\gamma,\beta_l,\beta_r) = \begin{cases} \frac{\gamma}{(\beta_l+\beta_r)\Gamma\left(\frac{1}{\gamma}\right)} \exp\left(-\left(\frac{-x}{\beta_l}\right)^{\gamma}\right) & x \le 0 \\ \frac{\gamma}{(\beta_l+\beta_r)\Gamma\left(\frac{1}{\gamma}\right)} \exp\left(-\left(\frac{x}{\beta_r}\right)^{\gamma}\right) & x > 0 \end{cases} \tag{18}$$

where the mean of the distribution is:

$$\eta = (\beta_r - \beta_l)\frac{\Gamma\left(\frac{2}{\gamma}\right)}{\Gamma\left(\frac{1}{\gamma}\right)} \tag{19}$$

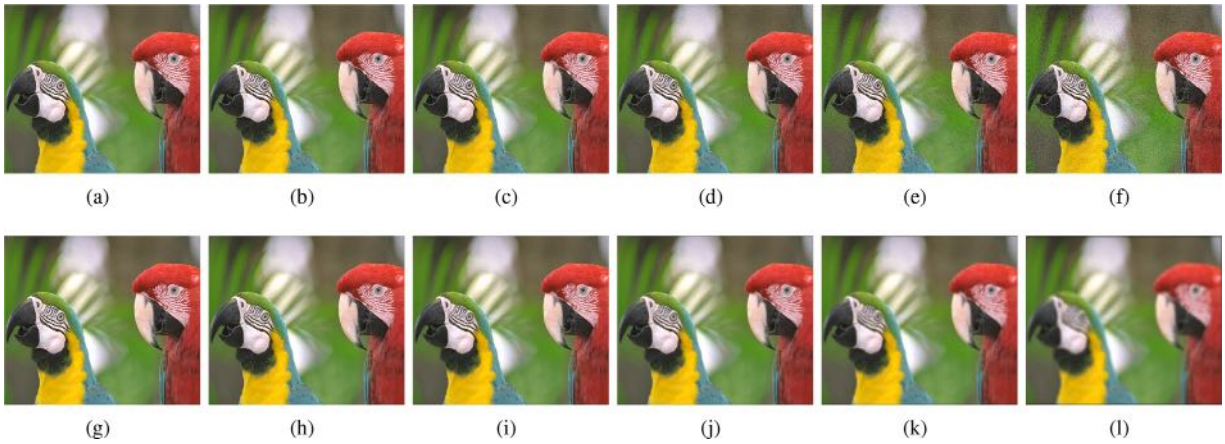

Fig. 4. (a) and (g) are the high quality images. (b)–(f) are the five levels AGN-distorted images, and (h)–(l) are the five levels GB-distorted images.

The distribution parameters (γ, β_l, β_r, η) are also incorporated as quality-aware features. Note that the same conclusion can also be obtained for other orientations. Each orientation can obtain the four distribution parameters. Overall, totally 18 features are obtained from the QMSCN and adjacent QMSCN maps. The extracted features on naturalness are summarized as $f_{QMSCN} = \{\alpha, \beta, (\gamma, \beta_l, \beta_r, \eta)_{\times 4}\}$.

3.3. Quaternion structure statistics modelling

The image structure is proven to be an effective feature in IQA modelling [21,22]. In this paper, we employed the image gradient in quaternion domain to describe the local contrast and structure. The horizontal $\ddot{h}_x$ and vertical $\ddot{h}_y$ quaternion gradient operators are defined as:

$$\ddot{h}_x = \frac{1}{6}\begin{bmatrix} \ddot{u} & \ddot{u}_0 & \ddot{u}^* \\ \ddot{u} & \ddot{u}_0 & \ddot{u}^* \\ \ddot{u} & \ddot{u}_0 & \ddot{u}^* \end{bmatrix} \quad \ddot{h}_y = \frac{1}{6}\begin{bmatrix} \ddot{u} & \ddot{u} & \ddot{u} \\ \ddot{u}_0 & \ddot{u}_0 & \ddot{u}_0 \\ \ddot{u}^* & \ddot{u}^* & \ddot{u}^* \end{bmatrix} \tag{20}$$

where $\ddot{u} = \frac{1}{\sqrt{3}}(i + j + k)$ is a unit pure quaternion, $\ddot{u}^* = \frac{1}{\sqrt{3}}(-i - j - k)$ is the conjugate of $\ddot{u}$, and $\ddot{u}_0 = 0$. Then, the gradients on the horizontal QG_x and vertical QG_y are computed as:

$$\begin{aligned} QG_x &= \sqrt{(\ddot{I} \otimes \ddot{h}_x) \cdot (\ddot{I} \otimes \ddot{h}_x)^*} \\ QG_y &= \sqrt{(\ddot{I} \otimes \ddot{h}_y) \cdot (\ddot{I} \otimes \ddot{h}_y)^*} \end{aligned} \tag{21}$$

where "$\otimes$" denotes the convolution operation. Fig. 3(d) and (e) illustrates the QG_x and QG_y maps of Fig. 1(a), and Fig. 1(i) and (j) shows the distributions of QG_x and QG_y, respectively. The gradient map can be fitted with the Weibull distribution as:

$$f(x; \lambda, k) = \begin{cases} \frac{k}{\lambda}\left(\frac{x}{\lambda}\right)^{k-1} \exp\left(-\left(\frac{-x}{\lambda}\right)^k\right) & x \geq 0 \\ 0 & x < 0 \end{cases} \tag{22}$$

The distribution descriptors λ and k are chosen as structural indicators. The four extracted quality-aware features of the structure are summarized as $f_{QGM} = \{(\lambda, k)_{\times 2}\}$

3.4. Quaternion texture statistics modelling

Since the human eye perceives an image in multiple scales and multiple orientations [40], incorporating the multi-orientation features into IQA modelling is necessary. Log-Gabor is an effective multi-scale and multi-orientation image texture analysis tool and has been widely used in image identification [41], classification [42] and quality evaluation [43]. In this paper, Log-Gabor filters in the quaternion domain are employed to extract texture statistics features. The 2D Log-Gabor filter in the quaternion domain can be defined as:

$$Q\ddot{G}F(f, \theta) = \ddot{u} \cdot e^{-\frac{[ln(f/f_u)]^2}{2[(ln\sigma_f/f_u)]^2}} e^{-\frac{(\theta-\theta_v)^2}{2\sigma_\theta^2}} \tag{23}$$

where $f_t, t = 0, \ldots, T-1$ is the center frequency and $\theta_v = v\pi/V, v = 0, 1, \ldots, V-1$ is the orientation angle. We can obtain a set of Log-Gabor filters response with different center frequency and orientation angle. In this paper, we chose T=3, V=4. Therefore, we can obtain totally 12 quaternion Log-Gabor filter responses, and were denoted as $Q\ddot{G}R_{\{t,v\}}$ with $t = 1, 2, 3$ and $v = 1, 2, 3, 4$. The magnitude of the response are computed as:

$$QGabor\{t, v\} = \sqrt{Q\ddot{G}R\{t, v\} \cdot Q\ddot{G}R\{t, v\}^*} \tag{24}$$

Fig. 3(f) illustrates the quaternion Log-Gabor response of Fig. 3(a) with $t = 0, v = 0$. Fig. 3(k) shows the distributions. The response can be well modelled by Weibull distribution. The distribution descriptors λ and k are chosen as the quality-aware features. The same conclusions can be obtained from other responses. Therefore, a totally of 24 features are obtained and summarized as $f_{QGB} = \{(\lambda, k)_{\times 12}\}$.

In summary, 18, 4 and 24 features are extracted on Naturalness, Structure and Texture, respectively. Furthermore, considering that the viewing distance and image resolution greatly influence the evaluated quality score, a multi-scale strategy is adopted to extract the features on the initial and the down-sampled scales [20–22]. Therefore, for an image, a total of (18 + 4 + 24) × 2=92 features are extracted for quality evaluation, which can be expressed as:

$$f = \{f_{QMSCN}, f_{QGM}, f_{QGB}\}_{\times 2} \tag{25}$$

3.5. Validation for extracted features

To validate the effectiveness of the quality-aware features in capturing the image degradation, we calculate the feature values with respect to different distortion levels. The first and second rows in Fig. 4 illustrate a reference and five distorted level images with the distortion types are Addictive Gaussian Noise (AGN) (the first row in Fig. 4) and Gaussian blur (GB) (the second row in Fig. 4) from the TID2013 database [37]. Fig. 5 shows the values of quality-aware features changing along the distortion levels. Note that the feature can be viewed as an effective feature if the values monotonously change with the distortion level. In Fig. 5, it can be seen that the estimated feature scores basically changed along with the distortion levels, which indicates that the quality-aware features can effectively distinguish the distortion level of the image.

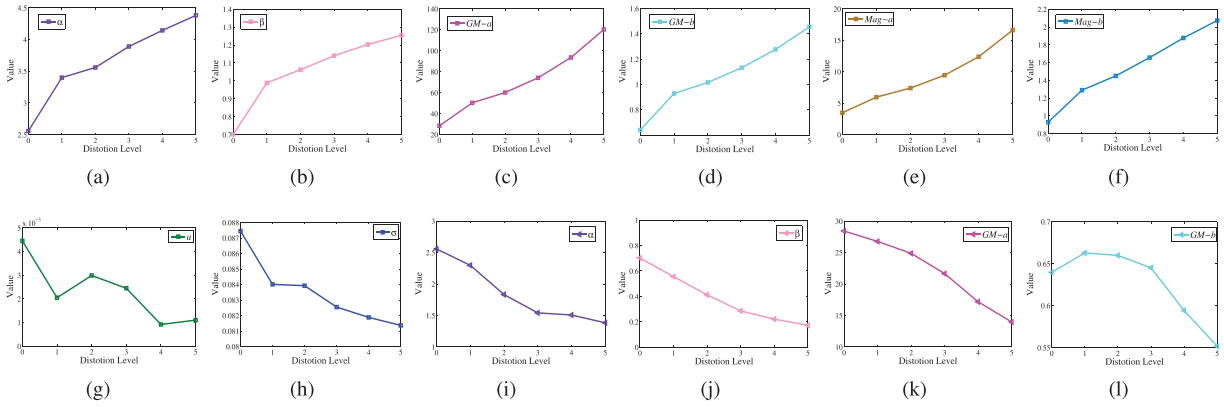

Fig. 5. The first and second rows are the quality-aware feature values changed along the AGN-distorted and GB-distorted images in Fig. 4, respectively.

4. The evaluation of the proposed method

The proposed Q-NIQE and competing models are evaluated in this section. First, the experimental protocols are reported. Then, the proposed Q-NIQE with competing methods are evaluated from three aspects: (1) prediction accuracy, (2) computational cost, and (3) robustness.

4.1. Experimental protocols

Eleven representative NR approaches containing six supervised and five unsupervised are compared to our model. The supervised methods include six mainstream NR methods: BIQI [8], DIIVINE [10], BRISQUE [12], BLINDS-II [11], NFERM [13], and multi-task end-to-end optimized deep neural network (MEON) [17]. The unsupervised methods include five classical methods: QAC [18], LPSI [19], NIQE [20], IL-NIQE [21] and SNP-NIQE [22].

Four commonly used indicators Spearman rank order correlation coefficient (SRCC), Kendalls rank correlation coefficient (KRCC), Pearson linear correlation coefficient (PLCC) and root mean square error (RMSE) are employed to quantify the prediction performances of the competing BIQA methods. Higher SRCC, KRCC and PLCC values and lower RMSE values indicate better IQA metrics. Before calculating the PLCC and RMSE, the object scores are mapped to subject scores via nonlinear regression [44], which can be implemented by a five-parameter logistic function:

$$q(x) = \chi_1\left(\frac{1}{2} - \frac{1}{1+\exp\left(\chi_2 \cdot (x-\chi_3)\right)}\right) + \chi_4 \cdot x + \chi_5 \tag{26}$$

where x and $q(x)$ are the objective score and the mapped score, and $\chi_{1,\ldots,5}$ are the five parameters to be fitted.

In the experiments, five colour databases are used for evaluation. Among them, LIVE [45], CSIQ [46], TID2013 [37] and IVC [47] databases are man-made databases. The distorted images are obtained by introducing distortions onto high-quality photographs. We selected the most common distortion types for evaluation as in [13,22]. LIVE In the Wild Image Quality Challenge Database (LIVE challenge) [48] is a real-world database that contains uncommon and multiple distortions. We employed it to test the generalization capability of the BIQA models. The detailed information of the databases is shown in Table 1.

To obtain the overall performance on the test databases, the weighted-average is adopted, which uses the number of images in each database as the weighting function to weight the measure index. The weighted-average is denoted as "AVG".

4.2. Prediction accuracy

Table 2 lists the prediction accuracy results of the Q-NIQE and unsupervised methods on the five databases. For each measure index, the best and second results are highlighted in red and blue, respectively. '—' indicates that the data are inaccessible. It can be seen from Table 2 that Q-NIQE performance is consistent well across all databases. In particular, Q-NIQE achieves the best results on LIVE challenge databases, which reveals that Q-NIQE has good generalization capability for multiple and real distortions. Overall, Q-NIQE achieves the best results on each measure index compared with existing state-of-the-art unsupervised methods.

Then, Q-NIQE is compared with supervised methods. Considering that the supervised methods need opinion scores for training before implementation, we train them on one dataset, and test them on other datasets. Note that the training step is not needed for Q-NIQE. To fully test the generalization capability performance of a supervised IQA model, the supervised IQA models are trained on LIVE and TID2013 databases, respectively. The number of images in LIVE database is larger than that in TID2013 database. The tested results are illustrated in Tables 3 and 4. For the sake of fairness, we optimized the parameters of all competing models in training. When the supervised methods are trained on LIVE database, it can be found that MEON model achieves the best results on CSIQ and TID2013 databases, NFERM model achieves the best results on IVC database, and the proposed model Q-NIQE achieves the best results on LIVE challenge database. However, when the supervised methods are trained on TID2013 database, the proposed Q-NIQE method achieves the best results among all databases. The performance of supervised methods decreases significantly compared with those trained on LIVE database. This is mainly caused by the decrease in the number of training images. The performance of the supervised methods heavily relies on the numbers of training images. Therefore, to obtain high prediction accuracy, the supervised method requires a larger number of images for training. However, obtaining a subjective quality score is rather time-consuming and costly. In contrast, the unsupervised method does not require labelled images for training, and therefore has a stable and robust application result. Specially, whether trained on LIVE or on TID2013 databases, Q-NIQE exhibits much better performance in LIVE challenge database than all supervised methods, which indicates that Q-NIQE has better generalization capability in application.

For visualization, Fig. 6 shows the scatter plots of subjective MOS/DMOS values versus objective values obtained from QAC, NIQE, IL-NIQE, SNP-NIQE and the proposed Q-NIQE on LIVE, CSIQ, TID2013 and LIVE challenge databases. For a more comprehensive analysis, different distortion types are marked with distinct

Table 1
Main information about tested image quality databases.

Database	LIVE	CSIQ	TID2013	IVC	LIVE challenge
Number of reference images	29	30	25	10	None
Number of distorted images	779	600	500	120	1162
Distortion types	FF, GB, WN JP2K, JPEG	GB, AWGN JP2K, JPEG	AGN, GB JPEG, JP2K	JPEG, GB JP2K	Multiple distortions
Number of observers	161	35	917	15	8100
Size of images	480 × 720, etc.	512 × 512	512 × 384	512 × 512	500 × 500

Table 2
Evaluation results compared with unsupervised methods.

Database	Index	QAC[18]	LPSI[19]	NIQE[20]	IL-NIQE[21]	SNP-NIQE[22]	Q-NIQE(pro.)
LIVE	SRCC	0.8443	0.8181	0.9062	0.8971	**0.9082**	**0.9113**
	KRCC	0.6443	0.6175	0.7273	0.7116	**0.7366**	**0.7323**
	PLCC	0.7575	0.8280	0.9039	0.9020	**0.9069**	**0.9077**
	RMSE	17.8371	15.3184	11.6852	11.7972	**11.5116**	**11.4622**
CSIQ	SRCC	0.8364	0.7711	0.8707	0.8800	**0.9009**	**0.9046**
	KRCC	0.6272	0.5826	0.6848	0.6975	**0.7210**	**0.7216**
	PLCC	0.8474	0.8657	0.8754	0.9066	**0.9064**	**0.9126**
	RMSE	0.1500	0.1415	0.1366	0.1193	**0.1194**	**0.1157**
TID2013	SRCC	0.7862	0.7046	0.7940	0.8421	**0.8565**	**0.8586**
	KRCC	0.5941	0.5005	0.5898	0.6536	**0.6583**	**0.6562**
	PLCC	0.7801	0.8114	0.8005	0.8582	**0.8470**	**0.8576**
	RMSE	0.8726	0.8153	0.8276	0.7461	**0.7416**	**0.7174**
IVC	SRCC	0.7672	—	0.7836	**0.8512**	0.8379	**0.8596**
	KRCC	0.5585	—	0.5942	**0.6582**	0.6515	**0.6717**
	PLCC	0.7481	—	0.7897	**0.8606**	0.8207	**0.8735**
	RMSE	0.7801	—	0.7619	**0.6324**	1.7068	**0.6047**
LIVE challenge	SRCC	0.0782	—	0.4512	0.4390	**0.4662**	**0.5203**
	KRCC	0.0579	—	0.3073	0.2983	**0.3165**	**0.3594**
	PLCC	0.2408	—	0.4975	0.5046	**0.5182**	**0.5619**
	RMSE	19.6818	—	17.5903	17.5073	**17.3114**	**16.7739**
AVG	SRCC	0.5491	—	0.7098	0.7150	**0.7335**	**0.7560**
	KRCC	0.4143	—	0.5380	0.5458	**0.5636**	**0.5789**
	PLCC	0.5913	—	0.7284	0.7483	**0.7512**	**0.7723**

Table 3
Evaluation results compared with supervised methods when trained on LIVE.

Database	Index	BIQI[8]	DIIVINE[10]	BISQUE[12]	BLINDS-II[11]	NFERM[13]	MEON[17]	Q-NIQE(pro.)
CSIQ	SRCC	0.6152	0.8718	0.8903	0.8797	**0.9057**	**0.9300**	0.9046
	KRCC	0.4367	0.6849	0.7154	0.6987	**0.7360**	**0.7656**	0.7216
	PLCC	0.6197	0.9002	0.9158	0.9111	**0.9374**	**0.9422**	0.9126
	RMSE	0.2218	0.1230	0.1135	0.1165	**0.0984**	**0.0947**	0.1157
TID2013	SRCC	0.5475	0.8088	0.8029	0.7697	0.8254	**0.9012**	**0.8586**
	KRCC	0.3842	0.6121	0.6026	0.5885	0.6273	**0.7189**	**0.6562**
	PLCC	0.5654	0.8231	0.8022	0.7936	0.8333	**0.8939**	**0.8576**
	RMSE	1.0895	0.7502	0.7886	0.8014	0.7308	**0.6252**	**0.7174**
IVC	SRCC	0.4104	0.2548	0.8135	0.8667	**0.9177**	**0.9033**	0.8596
	KRCC	0.2860	0.3686	0.6150	0.6706	**0.7487**	**0.7278**	0.6717
	PLCC	0.4052	0.5436	0.8246	0.8709	**0.9272**	**0.8948**	0.8735
	RMSE	1.1353	1.0423	0.7025	0.6104	**0.4651**	**0.5545**	0.6047
LIVE challenge	SRCC	**0.4522**	0.2332	0.3711	0.2103	0.3630	0.3646	**0.5203**
	KRCC	**0.3061**	0.1571	0.2529	0.1431	0.2445	0.2454	**0.3594**
	PLCC	**0.4805**	0.0247	0.4013	0.2101	0.3971	0.4093	**0.5619**
	RMSE	**17.7841**	20.2782	18.5738	19.8257	18.6189	18.5184	**16.7739**
AVG	SRCC	0.5112	0.5160	0.6148	0.5294	0.6247	**0.6468**	**0.7052**
	KRCC	0.4662	0.3962	0.5334	0.4031	0.4741	**0.5001**	**0.5287**
	PLCC	0.5296	0.4390	0.6364	0.5424	0.6515	**0.6697**	**0.7280**

Table 4
Evaluation results compared with supervised methods when trained on TID2013.

Database	Index	BIQI[8]	DIIVINE[10]	BISQUE[12]	BLINDS-II[11]	NFERM[13]	MEON[17]	Q-NIQE(pro.)
LIVE	SRCC	0.5185	0.7781	**0.8441**	0.6750	0.8360	0.7917	**0.9113**
	KRCC	0.3548	0.5693	**0.6485**	0.4890	0.6409	0.5829	**0.7323**
	PLCC	0.4806	0.7703	0.7683	0.6996	**0.8413**	0.7869	**0.9077**
	RMSE	23.9603	17.4243	17.4873	19.5229	**14.9904**	16.8604	**11.4622**
CSIQ	SRCC	0.4902	0.7951	0.8212	**0.8716**	0.8536	0.7414	**0.9046**
	KRCC	0.3276	0.5803	0.6096	**0.6837**	0.6447	0.5537	**0.7216**
	PLCC	0.4204	0.8020	0.8335	**0.8937**	0.8694	0.8103	**0.9126**
	RMSE	0.2564	0.1688	0.1561	**0.1268**	0.1396	0.1656	**0.1157**
IVC	SRCC	0.3314	0.5334	0.4665	**0.8538**	0.8255	0.7960	**0.8596**
	KRCC	0.2340	0.3706	0.3388	**0.6675**	0.6246	0.5864	**0.6717**
	PLCC	0.4221	0.5602	0.4883	**0.8549**	0.8359	0.8162	**0.8735**
	RMSE	1.1256	1.0287	1.0837	**0.6444**	0.6817	0.7176	**0.6047**
LIVE challenge	SRCC	0.4071	**0.4850**	0.3201	0.2342	0.1186	0.2010	**0.5203**
	KRCC	0.2747	**0.3314**	0.2183	0.1563	0.0773	0.1351	**0.3594**
	PLCC	0.4360	**0.5195**	0.3642	0.3170	0.2732	0.2365	**0.5619**
	RMSE	18.2492	**17.3277**	18.8861	19.2323	19.507	19.7209	**16.7739**
AVG	SRCC	0.4550	**0.6429**	0.5931	0.5349	0.5262	0.5226	**0.7367**
	KRCC	0.3082	**0.4589**	0.4379	0.3957	0.3949	0.3809	**0.5734**
	PLCC	0.4449	**0.6585**	0.5939	0.5833	0.6037	0.5531	**0.7563**

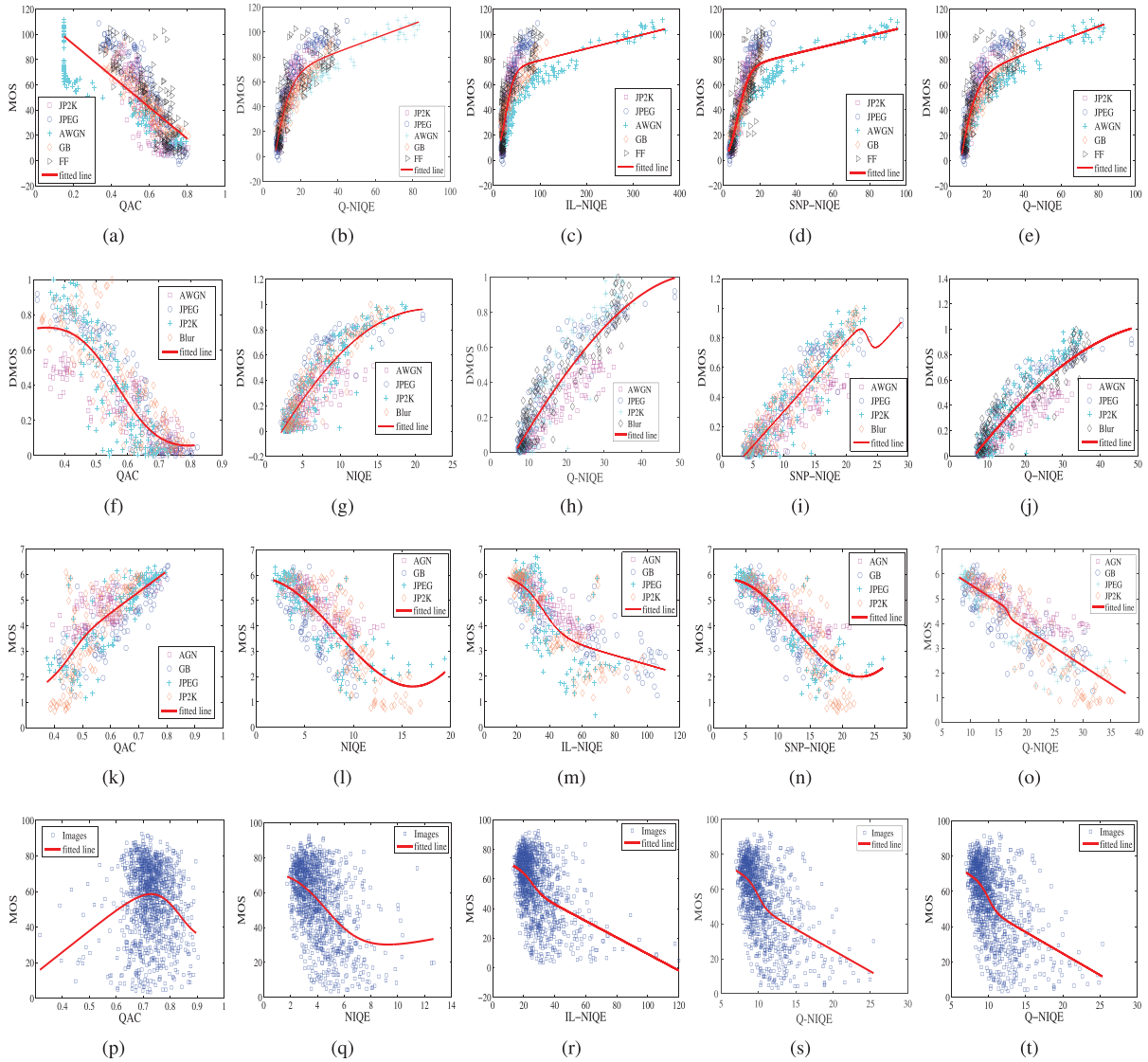

Fig. 6. Scatter plots of subjective scores against objective scores calculated by QAC, NIQE, IL-NIQE, Q-NIQE model on LIVE (first row), CSIQ (second row), TID2013 (third row) and LIVE challenge (last row) databases. Different types of distortions are marked by distinct colours.

Table 5
Performance and time-costing of features and their combinations in.

Features	f_{QMSCN}	f_{QMSCN} $+f_{QGM}$	f_{QMSCN} $+f_{QGM}+f_{QGB}$
SRCC	0.7114	0.9027	0.9113
Running times	1.7284	2.5826	5.4721

colours. Note that for a good IQA metric, the points should be clustered along the fitted line for distinct types of distortions. In Fig. 6, it can be seen that the scatter points of the Q-NIQE are clustered together for distinct types of distortions and show better consistency with MOS/DMOS than other methods. For instance, for Q-NIQE, the points on LIVE database are clustered well along the fitted line, and an obvious tendency is observed that the DMOS increases with the increase of the Q-NIQE assessed values. Nevertheless, for other testing IQA metrics, the points are relatively decentralized compared to Q-NIQE.

To examine the effectiveness of each type of feature, additional experiments are conducted using features and their combinations in. QMSCN is set as the basic feature, and the other features are added in turn. The performance (SRCC and time-costing are used) on each image is illustrated in Table 5. The prediction accuracy is continuously improved with the added features, which indicates that the features utilized in Q-NIQE are significant.

4.3. Computational complexity

The computational cost of each BIQA model is measured in terms of the time cost on each image. Each BIQA model is tested on the whole LIVE database ten times and the average value is calculated as the measure index. These experiments are performed on a Dell workstation with a 3.2 GHz Intel Core $i7^{TM}$ processor and a 16 GB RAM. The software platform is Matlab R2010b. The results of average time costing on each image are listed in Table 6. Generally, compared with the models with similar prediction accuracy (e.g., IL-NIQE, SNP-NIQE, NFERM), Q-NIQE has the modest computational complexity.

4.4. Quaternion representation validation

To test the effectiveness of the quaternion representation, the performances of the proposed quaternion-based model Q-NIQE and the single channel (i.e., R, G, B channels) based models as well as the channels combined model are reported. We name the trained model on the R, G, and B channels as R-NIQE, G-NIQE, and B-NIQE, respectively. For example, R-NIQE denotes the features are extracted on the R channel. We also extract the features on the R, G, and B channels. The extracted features are then concatenated to modelling. The established model is referred as RGB-NIQE. The prediction accuracy results are shown in Table 7. For each index, the model achieved the best results is highlighted in boldface. Q-NIQE achieves the best performance almost on each database except CSIQ database. Overall, Q-NIQE achieves the best results on each measure index.

In addition, the computational cost of R-NIQE, G-NIQE, B-NIQE, RGB-NIQE, and Q-NIQE models is measured in terms of the time cost on each image. The results are shown in Table 8. The proposed

Table 7
The prediction accuracy of the R-NIQE, G-NIQE, B-NIQE, RGB-NIQE, and Q-NIQE models.

Database	Index	R-NIQE	G-NIQE	B-NIQE	RGB-NIQE	Q-NIQE
LIVE	SRCC	0.8745	0.8766	0.8787	0.8529	**0.9113**
	KRCC	0.6814	0.6832	0.6859	0.6554	**0.7323**
	PLCC	0.8792	0.8802	0.8836	0.8619	**0.9077**
CSIQ	SRCC	0.9141	**0.9162**	0.9104	0.8418	0.9046
	KRCC	0.7437	**0.7480**	0.7397	0.6471	0.7216
	PLCC	0.9227	0.9276	**0.9397**	0.8726	0.9126
TID2013	SRCC	0.8432	0.8436	0.8355	0.8046	**0.8586**
	KRCC	0.6485	0.6498	0.6408	0.6067	**0.6562**
	PLCC	0.8704	0.8736	0.8611	0.8277	**0.8578**
IVC	SRCC	0.8385	0.8496	0.8554	0.6940	**0.8596**
	KRCC	0.6408	0.6563	0.6605	0.5009	**0.6717**
	PLCC	0.8170	0.8401	0.8384	0.7031	**0.8576**
LIVE challenge	SRCC	0.4788	0.4934	0.4795	0.4809	**0.5203**
	KRCC	0.3263	0.3369	0.3263	0.3335	**0.3594**
	PLCC	0.5236	0.5401	0.5308	0.5211	**0.5619**
AVG	SRCC	0.7302	0.7370	0.7303	0.7004	**0.7560**
	KRCC	0.5559	0.5619	0.5558	0.5219	**0.5789**
	PLCC	0.7530	0.7616	0.7593	0.7272	**0.7723**

Table 8
The computational cost of Q-NIQE, R-NIQE, G-NIQE, B-NIQE, and RGB-NIQE models.

Method	Running times
R-NIQE	3.4090
G-NIQE	3.4144
B-NIQE	3.4263
RGB-NIQE	9.5411
Q-NIQE	5.4723

Q-NIQE model shows higher computational cost compared with R-NIQE, G-NIQE, and B-NIQE models, while shows much lower computational cost than RGB-NIQE. From Tables 7 and 8, it can be seen that using quaternion representation, better performance can be achieved without great time cost increasing.

4.5. Robustness test

We evaluate the robustness of the proposed IQA method from two aspects: (1) the sensitivity to the parameters and (2) the dependence on the pristine training images. SRCC is used as the performance index. First, we test the sensitivity to the parameters of the proposed method. Two parameters are involved, including the patch size s and the threshold Th when learning the MVG model. Fig. 7 illustrates the SRCC on the four databases under various s and Th. In Fig. 7(a), Th is fixed as 0.78 (the value set in IL-NIQE) and s ranges from 48 to 96 with an interval of 8. In Fig. 7(b), s is fixed as 64 and Th ranges from 0.6 to 0.9 with an interval of 0.05. It can be seen that the the performance of Q-NIQE is consistently good on the four databases under a wide range of parameter values.

Then, cross validation is used to test the dependence on the pristine training images. We train the NIQE model, IL-NIQE model and the proposed Q-NIQE model under the NIQE pristine images, IL-NIQE pristine images and the pristine images used in this paper, respectively. Table 9 illustrates the results of SRCC value on LIVE database. The performance of Q-NIQE is consistently good com-

Table 6
Computational cost of the tested models on LIVE database.

Metrics	BIQI	DIIVINE	BLINDS-II	BRISQUE	NFERM	MEON	QAC	NIQE	IL-NIQE	SNP-NIQE	Q-NIQE
Running times	0.14	22.12	83.59	0.51	57.17	0.098	0.42	0.38	9.56	4.83	5.47

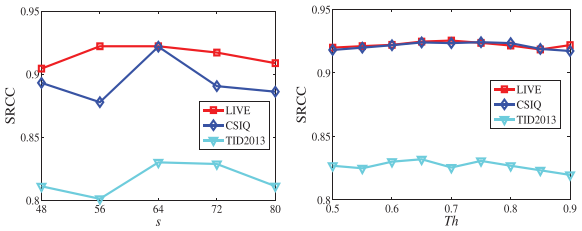

Fig. 7. Robustness test of the proposed method in terms of the sensitivity to parameters (a) patch size *s*, (b) threshold *Th*.

Table 9
Cross validation for robustness test.

Pristine images	NIQE	IL-NIQE	Q-NIQE
NIQE	0.9062	0.9002	0.8942
IL-NIQE	0.9015	0.8971	0.8500
Q-NIQE	0.9145	0.9062	0.9113

pared with that of NIQE and IL-NIQE, which indicates that the proposed model has better robustness than NIQE and IL-NIQE.

Conclusion

Processing colour information properly and incorporating it into IQA modelling is a vital and meaningful task as we lived in a colourful world. However, existing methods, whether converting a colour image into greyscale methods, or extracting features on each channel of the colour image methods, cannot reflect the correlation between different colour channels. This paper proposes an efficient unsupervised methods based on quaternion representation. By encoding the three channels of an RGB colour image into the three imaginary parts of a quaternion, the colour image can be processed as a whole and can effectively reflect the correlation between different colour channels. Naturalness statistic features, structure statistic features and texture statistic features are extracted in the quaternion domain to establish a MVG model. The quality of a distorted image is calculated by measuring the MVG variations between fitted for distorted image and fitted for pristine natural images. The performance evaluated on LIVE, TID2013, CSIQ, IVC and LIVE challenge databases demonstrates the high efficiency in capturing the image degradation of Q-NIQE. In the future, we intend to propose an efficient unsupervised BIQA method since existing methods usually have high computational complexity.

Declaration of Competing Interest

The authors declare that they have no known competing financial interests or personal relationships that could have appeared to influence the work reported in this paper.

CRediT authorship contribution statement

Leyuan Wu: Resources, Writing - original draft, Software, Investigation. **Xiaogang Zhang:** Supervision, Visualization. **Hua Chen:** Project administration, Conceptualization. **Yicong Zhou:** Methodology, Validation.

Acknowledgements

This research was supported by the National Key R&D Program of China under Grant 2018YFB1305900.

References

[1] A.C. Bovik, Automatic prediction of perceptual image and video quality, Proc. IEEE 101 (2013) 2008–2024.
[2] Z. Wang, A.C. Bovik, H.R. Sheikh, E.P. Simoncelli, Image quality assessment: from error visibility to structural similarity, IEEE Trans. Image Process. 13 (4) (2004) 600–612.
[3] S. Liu, Z. Huang, Efficient image hashing with geometric invariant vector distance for copy detection, ACM Trans. Multimed. Comput. Commun. Appl. (TOMM) 15 (4) (2019).
[4] Z. Tang, Z. Huang, H. Yao, X. Zhang, L. Chen, C. Yu, Perceptual image hashing with weighted DWT features for reduced-reference image quality assessment, Comput. J. (2018).
[5] L. Wu, X. Zhang, H. Chen, Effective quality metric for contrast-distorted images based on SVD, Signal Process. Image Commun. 78 (2019) 254–262.
[6] R. Ferzli, L.J. Karam, A no-reference objective image sharpness metric based on the notion of just noticeable blur (JNB), IEEE Trans. Image Process. 18 (4) (2009) 717–728.
[7] F. Pan, et al., A locally adaptive algorithm for measuring blocking artifacts in images and videos, Signal Process. Image Commun. 19 (6) (2004) 499–506.
[8] A.K. Moorthy, A.C. Bovik, A two-step framework for constructing blind image quality indices, IEEE Signal Process. Lett. 17 (5) (2010) 513–516.
[9] M.A. Saad, A.C. Bovik, C. Charrier, A DCT statistics-based blind image quality index, IEEE Signal Process. Lett. 17 (6) (2010) 583–586.
[10] A.K. Moorthy, A.C. Bovik, Blind image quality assessment: from natural scene statistics to perceptual quality, IEEE Trans. Image Process. 20 (12) (2011) 3350–3364.
[11] M.A. Saad, A.C. Bovik, C. Charrier, Blind image quality assessment: a natural scene statistics approach in the DCT domain, IEEE Trans. Image Process. 21 (8) (2012) 3339–3352.
[12] A. Mittal, A.K. Moorthy, A.C. Bovik, No-reference image quality assessment in the spatial domain, IEEE Trans. Image Process. 21 (12) (2012) 4695–4708.
[13] K. Gu, G. Zhai, X. Yang, W. Zhang, Using free energy principle for blind image quality assessment, IEEE Trans. Multimed. 17 (1) (2015) 50–63.
[14] Q. Wu, H. Li, F. Meng, K.N. Ngan, B. Luo, C. Huang, B. Zeng, Blind image quality assessment based on multichannel feature fusion and label transfer, IEEE Trans. Circuits Syst. Video Technol. 26 (3) (2016) 425–440.
[15] J. Kim, A. Nguyen, S. Lee, Deep CNN-based blind image quality predictor, IEEE Trans. Neural Netw. Learn. Syst. 30 (1) (2019) 11–24.
[16] W. Zhang, K. Ma, J. Yan, D. Deng, Z. Wang, Blind image quality assessment using a deep bilinear convolutional neural network, IEEE Trans. Circuits Syst. Video Technol. 30 (1) (2020) 36–47.
[17] K. Ma, W. Liu, K. Zhang, Z. Duanmu, Z. Wang, W. Zuo, End-to-end blind image quality assessment using deep neural networks, IEEE Trans. Image Process. 27 (3) (2018) 1202–1213.
[18] W. Xue, L. Zhang, X. Mou, Learning without human scores for blind image quality assessment, in: Proceedings of the 2013 IEEE Conference on Computer Vision and Pattern Recognition, 2013, pp. 995–1002.
[19] Q. Wu, Z. Wang, H. Li, A highly efficient method for blind image quality assessment, in: Proceedings of the 2015 IEEE International Conference on Image Processing (ICIP), 2015, pp. 339–343.
[20] Q. Wu, Z. Wang, H. Li, A highly efficient method for blind image quality assessment, in: Proceedings of the 2015 IEEE International Conference on Image Processing (ICIP), 2015, pp. 339–343.
[21] L. Zhang, L. Zhang, A.C. Bovik, A feature-enriched completely blind image quality evaluator, IEEE Trans. Image Process. 24 (8) (2015) 2579–2591.
[22] Y. Liu, K. Gu, Y. Zhang, X. Li, G. Zhai, D. Zhao, W. Gao, Unsupervised blind image quality evaluation via statistical measurements of structure, naturalness and perception, IEEE Trans. Circuits Syst. Video Technol. (2019). 1–1.
[23] Andreas Koschan, M. A. Abidi, *Digital Color Image Processing*, Wiley-Interscience, 2008.
[24] M. Wilson, M.A. Ali, M.A. Klyne, Vision in Vertebrates, BioScience 37 (6) (1987) 238–238.
[25] Q. Barthlemy, A. Larue, J.I. Mars, Color sparse representations for image processing: Review, models, and prospects, IEEE Trans. Image Process. 24 (11) (2015) 3978–3989.
[26] Y. Chen, X. Xiao, Y. Zhou, Low-rank quaternion approximation for color image processing, IEEE Trans. Image Process. 29 (2020) 1426–1439.
[27] R. Lan, Y. Zhou, Quaternion-Michelson descriptor for color image classification, IEEE Trans. Image Process. 25 (11) (2016) 5281–5292.
[28] C. Zou, K.I. Kou, Y. Wang, Quaternion collaborative and sparse representation with application to color face recognition, IEEE Trans. Image Process. 25 (7) (2016) 3287–3302.
[29] S. Gai, Z. Bao, K. Zhang, Vector extension of quaternion wavelet transform and its application to colour image denoising, IET Signal Process. 13 (2) (2019) 133–140.
[30] Y. Wang, W. Liu, Y. Wang, Color image quality assessment based on quaternion singular value decomposition, in: Proceedings of the 2008 Congress on Image and Signal Processing, 3, 2008, pp. 433–439.
[31] Qiwei Chen, Yi Xu, Chuan Li, Ning Liu, Xiaokang Yang, An image quality assessment metric based on quaternion wavelet transform, in: Proceedings of the 2013 IEEE International Conference on Multimedia and Expo Workshops (ICMEW), 2013, pp. 1–6.
[32] A. Kolaman, O. Yadid-Pecht, Quaternion structural similarity: A new quality index for color images, IEEE Trans. Image Process. 21 (4) (2012) 1526–1536.

[33] W. Hamilton, On quaternions; or on a new system of imaginaries in algebra, Dublin Philos. Mag. J. Sci. 25 (163) (1844) 10–13.
[34] D. Martin, C. Fowlkes, D. Tal, J. Malik, A database of human segmented natural images and its application to evaluating segmentation algorithms and measuring ecological statistics, in: Proceedings of the Eighth IEEE International Conference on Computer Vision, ICCV 2001, 2, 2001, pp. 416–423vol.2.
[35] D. Ruderman, The statistics of natural images, Netw. Comput. Neural Syst. 5 (1994) 517–548.
[36] S.J. Sangwine, Fourier transforms of colour images using quaternion or hypercomplex, numbers, Electron. Lett. 32 (21) (1996) 1979–1980.
[37] N. Ponomarenko, L. Jin, et al., Image database tid2013: Peculiarities, results and perspectives, Signal Process.: Image Commun. 30 (2015) 57–77.
[38] K. Sharifi, A. Leon-Garcia, Estimation of shape parameter for generalized gaussian distributions in subband decompositions of video, IEEE Trans. Circuits Syst. Video Technol. 5 (1) (1995) 52–56.
[39] N. Lasmar, Y. Stitou, Y. Berthoumieu, Multiscale skewed heavy tailed model for texture analysis, in: Proceedings of the 16th IEEE International Conference on Image Processing (ICIP), 2009, pp. 2281–2284.
[40] R.J.P. B. D. B. Willmore, J.L. Gallant, Neural representation of natural images in visual are v2, J. Neurosci. 30 (6) (2010) 2102–2114.
[41] J. Arróspide, L. Salgado, Log-Gabor filters for image-based vehicle verification, IEEE Trans. Image Process. 22 (6) (2013) 2286–2295, doi:10.1109/TIP.2013.2249080.
[42] F.H.C. Tivive, S.L. Phung, A. Bouzerdoum, Classification of micro-doppler signatures of human motions using Log-Gabor filters, IET Radar Sonar Navig. 9 (9) (2015) 1188–1195.
[43] H. Guo, K. Ma, H. Zeng, A Log-Gabor feature-based quality assessment model for screen content images, in: Proceedings of the 2019 IEEE International Conference on Image Processing (ICIP), 2019, pp. 4499–4503, doi:10.1109/ICIP.2019.8803491.
[44] H.R. Sheikh, M.F. Sabir, A.C. Bovik, A statistical evaluation of recent full reference image quality assessment algorithms, IEEE Trans. Image Process. 15 (11) (2006) 3440–3451.
[45] L.C.H.R. Sheikh,, Z. Wang, A. C.Bovik, Live Image Quality Assessment Database Release 2, (http://live.ece.utexas.edu/research/Quality/subjective.htm/).
[46] E.C. Larson, D. Chandler, Categorical Image Quality (CSIQ) Database, (Online, http://vision.okstate.edu/csiq).
[47] P. Le Callet, F. Autrusseau, Subjective quality assessment IRCCyN/IVC database, 2005, http://www.irccyn.ec-nantes.fr/ivcdb/.
[48] D. Ghadiyaram, A.C. Bovik, Massive online crowdsourced study of subjective and objective picture quality, IEEE Trans. Image Process. 25 (1) (2016) 372–387.